HHS Public Access

Author manuscript

Opt Lett. Author manuscript; available in PMC 2019 December 02.

Published in final edited form as:

Opt Lett. 2019 September 01; 44(17): 4219–4222. doi:10.1364/OL.44.004219.

Coextensive synchronized SLO-OCT with adaptive optics for human retinal imaging

Mehdi Azimipour[*,1], **Ravi S. Jonnal**[1], **John S. Werner**[1], **Robert J. Zawadzki**[1,2]

[1]Vision Science and Advanced Retinal Imaging Laboratory (VSRI), Department of Ophthalmology and Vision Science, UC Davis Eye Center

[2]EyePod Small Animal Ocular Imaging Laboratory, Department of Cell Biology and Human Anatomy, University of California Davis, Davis, CA, USA

Abstract

We describe the details of a multimodal retinal imaging system which combines adaptive optics (AO) with an integrated scanning light ophthalmoscopy (SLO) and optical coherence tomography (OCT) imaging system. The OCT subsystem consisted of a swept-source, Fourier domain mode-locked (FDML) laser, with a very high A-scan rate (1.6*MHz*), whose beam was raster scanned on the retina by two scanners–one resonant scanner and one galvanometer. The high sweep rate of the FDML permitted the SLO and OCT to utilize the same scanners for *in vivo* retinal imaging, and thus–unlike existing multimodal systems—concurrently acquired SLO frames and OCT volumes with approximate *en face* correspondence at a rate of 6*Hz*. The AO provided diffraction-limited cellular resolution for both imaging channels.

OCIS codes:

(010.1080) Active or adaptive optics; (170.4460) Ophthalmic optics and devices; (110.4500) Optical coherence tomography; (170.0110) Imaging systems; (170.4470) Ophthalmology

For more than a decade, two types of raster-scanned retinal imaging systems equipped with adaptive optics (AO) have been used to study the structure and function of the living human retina. The first of these is the AO scanning light ophthalmoscope (SLO)[1], in which light scattered by the retina is measured using a detector, while using a pinhole conjugated to the retina in order to reject out-of-focus and multiply-scattered light. The AO-SLO produces a two-dimensional, areal image of the retina with cellular resolution. It has been used to image the cone mosaic[1] and rod mosaic[2], and with modifications to the pinhole size and position and/or numbers of detectors, it has been used to image retinal vasculature in detail[3], cone inner segments[4], and inner retinal neurons[5]. The second raster-scanned AO imaging modality was optical coherence tomography (OCT), which permits volumetric imaging of the retina[6] including 3D images of single cells[7] when combined with AO[8, 9]. Each of these two modalities offers unique advantages, with SLO allowing detection of multiply scattered photons as well as fluorescently emitted ones and OCT allowing

*Corresponding author: Mehdi Azimipour, mazimipour@ucdavis.edu.

extraction of axial scattering profiles and sensitivity to sub-wavelength changes in the axial position of scattering structures. Because of its relatively small data size, real-time visualization of the AO-SLO image stream is computationally practical, whereas the large data size, dimensionality, and post-processing requirements hamper real-time visualization of the AO-OCT stream. Incorporating an SLO channel in the system permits visual validation of AO performance and rapid tuning of optical, electronic, and software parameters. The tractability of AO-SLO data also permits imaging and montaging over large fields of view. On the other hand, the AO-OCT provides a three-dimensional volume containing information about the amplitude and phase of the reflected light, the latter of which has been used effectively to measure blood flow[10], improve vascular contrast[11] and measure physiological changes in photoreceptors[12]. In the years since the emergence of AO-OCT[8, 9], a number of investigators have integrated SLO detection into AO-OCT systems[13-20]. However, due to the comparatively slow acquisition speeds of volumetric OCT images, fully spatiotemporally synchronized acquisition of OCT volumes and SLO frames has not yet been successfully achieved. From the outset, AO-SLO frames have been acquired at rates near $30 Hz$[1] with sampling rates of tens of megahertz. Acquisition speeds of OCT systems depend on the speed and sensitivity of the linescan camera (in spectrometer-based systems) or the sweep rate of the tunable laser (in swept-source systems). These characteristics are continually improving, and the recent advent of Fourier-domain mode-locked (FDML) swept-sources with sweep rates greater than $1 MHz$[21, 22] brings the sampling frequency of OCT significantly closer to that of SLO. In this letter, we introduce a combined AO-SLO-OCT system that leverages a $1.6 MHz$ FDML laser in order to acquire synchronized, coextensive OCT volumes and SLO frames. This mode of acquisition is significant because it broadens the scientific capabilities of the system while simplifying its optical design and data processing, by obviating separate scanning channels for OCT and SLO and producing corresponding images, respectively. The scientific benefits and practicality of our combined approach will grow with the speed of future swept-sources.

A schematic of the sample arm in the combined AO SLO-OCT system is shown in Fig. 1(A). The swept-source OCT system employed an FDML laser (FDM-1060-750-4B-APC, OptoRes GmbH, Munich, Germany) operating at an A-scan rate of $1.64 MHz$[21, 22]. The details of the OCT system can be found in[23]. In summary, a Michelson interferometer with three 50 : 50 fiber couplers was used to split the light between the sample and reference arm and the interference pattern was detected using a balanced detector, with a measured sensitivity of $-85 dB$. A dichroic mirror (zt1064rdc-sp, Chroma, USA) was employed to reflect the OCT beam while transmitting the SLO light. The scanning system contained a resonant scanner (SC-30, Electro-Optical Products Corp., Ridgewood, NY, USA) oscillating at $2 kHz$ in the horizontal direction and a galvanometer scanner in the slower vertical direction. The scanner configuration, in conjunction with the A-scan rate, permitted the acquisition of 6 volumes per second over a field of view of 1° × 1° (400 A-scans per B-scan and 340 B-scans per each volume). Because the laser has a fixed A-scan rate, a trade-off exists between spatial sampling density, field of view (FOV), and volume rate. An earlier version of the AO-OCT[23] employed a $5 kHz$ resonant scanner to achieve a $30 Hz$ volume rate but with a smaller FOV and lower density; future work with the present system requires this larger FOV and density, and will not be limited by the current $6 Hz$ volume rate. SLO

images were acquired by focusing light from a separate 840*nm* SLD source with 50*nm* full-width at half-maximum bandwidth (S840, Superlum Ltd, Moscow, Russia) on the retina. A wedged beam splitter was employed in front of the SLO fiber collimator to reflect 10 percent of the light toward the sample arm (BSN11, Thorlabs, USA). In the detection channel, the back-scattered light from the retina was spatially filtered using a confocal pinhole with a diameter of 0.5 Airy disk and was detected by a PMT (H7422P-50, Hamamatsu, Japan). The output of the PMT module was amplified using a high-speed current amplifier (HCA-10M-100K, Femto, Germany) and digitized by a frame grabber (ATS9440, AlazarTech, Canada). Table 1 summarizes the characteristics of both SLO and OCT systems and their data acquisition settings during imaging. The powers of the OCT and SLO beams were 1.8*mW* and 150μW at the cornea, respectively. Together, they are less than 50% of the maximum permissible exposure for 8 hours of continuous viewing as specified by ANSI. For typical experimental conditions of less than 120 seconds of continuous viewing, they are 16% of the MPE[24]. The data acquisition platforms for SLO and OCT were on two different computers and thus required synchronization of the channels during data recording. For this purpose, the OCT B-scan trigger signal was shared between the two digitizers and the OCT/SLO systems operated in master/slave configuration. During a one-way trip of the resonant scanner, the OCT digitizer captured a B-scan of 400 samples while the 20*MHz* SLO digitizer acquired a line scan of 4096 samples. This design permitted simultaneous acquisition for SLO and OCT channels (see Visualization 1). The AO subsystem incorporated a highspeed deformable mirror (DM-97-15; ALPAO SAS, Montbonnot-Saint-Martin, France) and a Shack–Hartmann wavefront sensor (SHWS) consisting of a 20 × 20 lenslet array (diameter 10*mm*; pitch 500μm; f = 30*mm*, Northrop-Grumman Corp, Arlington, VA,USA) in front of a sCMOS camera (Ace acA2040-180km; Basler AG). In this design, the SLO light also served as a SHWS beacon, where 8% of the light coming from the eye was reflected toward the SHWS using a beamsplitter. The system measured and corrected aberrations over a 6.75*mm* pupil in a closed-loop at a rate of 10*Hz*, yielding a theoretical diffraction-limited lateral resolution of 2.75μm and 3.2μm for the SLO and OCT channels, respectively. Custom software developed in Python/Cython controlled the AO loop[25]. After obtaining informed consent, two subjects free of known retinal disease were imaged. Each subject's eye was dilated and cyclopleged by instilling topical drops of 2.5% phenylephrine and 1% tropicamide. All procedures were in accordance with the tenets of the Declaration of Helsinki and were approved by the University of California, Davis Institutional Review Board. A bite-bar and forehead rest were used with a motorized X-Y-Z translation stage to position and stabilize the subject's pupil during imaging. To position the eye at specified retinal locations and also to reduce eye movements, a calibrated fixation target was employed during imaging. A dichroic mirror was placed in front of the pupil to combine the imaging with the fixation target beams. The average time for acquiring one data set, including the initial alignment was less than a minute with more than 2 minutes between the subsequent acquisitions. The post-processing of the acquired OCT data was done using custom software[26] developed in Matlab (The MathWorks, Inc., Natick, MA, USA) as was image segmentation and visualization. First, the volumetric images were segmented axially and the inner-outer segment (IS/OS) and cone outer segment tips (COST) layers were automatically identified and projected. A calibration grid target (R1L3S3P, Thorlabs, NJ, USA) was imaged prior to the experiments to compute and compensate for the

sinusoidal distortion of the images because of the use of the resonant scanner. A single projection was selected as a reference image, and the remaining target images were divided into strips of between 3 – 15 pixels of height and registered to the reference using a strip-based registration approach[12, 27, 28]. In Fig. 1, panels **(B)** and **(C)** show the motion-corrected average of 50 cone mosaic images from the foveal center and 1.75 degree temporal retina (TR) acquired by SLO and OCT channels, respectively. Despite being able to visualize cones at 1.75° with both AO-SLO and AO-OCT, the cones in the OCT *en-face* image, while having the same locations and density as those in the SLO image, appear larger in diameter. Their apparent size may also be affected by their waveguiding properties. In single mode fibers mode field diameter (MFD) increases with increasing wavelength. Foveal and parafoveal cones are thought to behave like single mode fibers, so the difference in wavelength between the two channels may cause a difference in their apparent size[29, 30]. As shwon in Fig. 2, panels **(A)** and **(B)**, the foveal cones are clearly visible in the AO-SLO image, but not in the AO-OCT image. Part of the apparent difference in foveal cone visibility is due to a wavelength-dependent difference in lateral resolution. It is also possible that coherent interference between cones, analogous to speckle noise, contributes to their reduced visibility in the OCT image, as described by Putnam *et al*.[31]. The same phenomenon may limit our ability to image the rod mosaic with OCT.

Multimodal systems with multiple imaging wavelengths suffer from longitudinal and transverse chromatic aberration (LCA and TCA, respectively). LCA is due to wavelength-dependence of focal length and can be compensated by adding defocus to one of the beams– here the OCT beam. In TCA, beams with different wavelengths focus in the same plane but with a lateral offset. While LCA is relatively constant for different imaging eccentricities, it has been shown that TCA varies for different eccentricities as the angle between the imaging beams and optical axis changes[32-34]. As shown in [34], beam position in the pupil can also impact TCA. To show the offset in our system, a small field of view of SLO and OCT images in Fig. 2(C) and (D) were color-coded and superimposed on top of each other before and after rigid-body registration and are shown in panels **(E)** and **(F)**, respectively. The 2D cross-correlation between the SLO and OCT channels indicates an offset of $19\mu m$ between the channels. It has been shown that TCA can result in beam displacements of several arcmin in the parafovea[33] over $300nm$ in the visible and NIR, which is roughly consistent with our finding. Additional potential sources of image misalignment are electronic latency between frame grabbers and misalignment of the beams in the pupil plane, the latter of which can exacerbate TCA. The displacement of spots on the retina is tantamount to a temporal delay between the images. In the worst case, when the displacement is in the slow (vertical) direction, $19\mu m$ corresponds to approximately $10ms$ of delay. In the images shown in Fig. 2, the delay was approximately $6ms$. This temporal delay or spatial offset may limit the precision of measurements requiring absolute synchronization; therefore, real-time TCA measurement and compensation may be required [34].

The SLO-OCT images acquired at 6° TR for the same subject are shown in Fig. 3. Single and motion-corrected average of 50 OCT *en-face* projections are shown in panels **(A)** and **(B)**, respectively. The corresponding single and averaged SLO frames are shown in panels **(C)** and **(D)**, respectively. A small region in both averaged images was magnified for better

visualization of rod and cone photoreceptors. For a detailed comparison between the spatial morphology of the photoreceptors in the AO-SLO and AO-OCT images, panel **(B)** and **(D)** were color-coded (SLO in magenta and OCT in green) and shown in pseudocolor composite in panel **(E)**. As demonstrated by panel **(E)**, there is correspondence between most of the cones, but not for rods. We believe that the difference in lateral resolution as well as coherent cross-talk (described above) may impede visualization of rods with the OCT.

In this letter, we have described results of a combined AO-SLO-OCT with coextensive, synchronized imaging. Synchronized imaging provides an avenue for a number of interesting experiments, but the precision of those measurements will be limited by TCA and alignment of the two beams.

Supplementary Material

Refer to Web version on PubMed Central for supplementary material.

Acknowledgments.

We thank Drs. Thomas Klein and Wolfgang Weiser from OptoRes GmbH for their extensive help with the FDML laser and providing the acquisition software. The authors also gratefully acknowledge the assistance of Justin V. Migacz, Denise Valente and Susan Garcia.

Funding. National Eye Institute (NEI) (R01-EY-026556, R01-EY-024239, P30-EY-012576, R00-EY-026068 and T32-EY-15387).

REFERENCES

1. Roorda A, Romero-Borja F, Donnelly W III, Queener H, Hebert T, and Campbell M, “Adaptive optics scanning laser ophthalmoscopy,” Opt Express 10, 405–412 (2002). [PubMed: 19436374]
2. Dubra A, Sulai Y, Norris J, Cooper R, Dubis A, Williams D, and Carroll J, “Noninvasive imaging of the human rod photoreceptor mosaic using a confocal adaptive optics scanning ophthalmoscope,” Biomed Opt Express 2, 1864–1876 (2011). [PubMed: 21750765]
3. Chui T, Gast TJ, and Burns SA, “Imaging of vascular wall fine structure in the human retina using adaptive optics scanning laser ophthalmoscopy,” Invest Ophth Vis Sci 54, 7115–24 (2013).
4. Scoles D, Sulai YN, Langlo CS, Fishman GA, Curcio CA, Carroll J, and Dubra A, “In vivo imaging of human cone photoreceptor inner segments,” Investig. ophthalmology & visual science 55, 4244–4251 (2014).
5. Rossi EA, Granger CE, Sharma R, Yang Q, Saito K, Schwarz C, Walters S, Nozato K, Zhang J, Kawakami T et al., “Imaging individual neurons in the retinal ganglion cell layer of the living eye,” Proc. Natl. Acad. Sci p. 201613445 (2017).
6. Huang D, Swanson EA, Lin CP, Schuman JS, Stinson WG, Chang W, Hee MR, Flotte T, Gregory K, Puliafito CA et al., “Optical coherence tomography,” Science. 254, 1178–1181 (1991). [PubMed: 1957169]
7. Jonnal RS, Kocaoglu OP, Zawadzki RJ, Liu Z, Miller DT, and Werner JS, “A review of adaptive optics optical coherence tomography: Technical advances, scientific applications, and the futurereview of adaptive optics optical coherence tomography,” Invest Ophth Vis Sci 57, OCT51–OCT68 (2016).
8. Zhang Y, Rha J, Jonnal RS, and Miller DT, “Adaptive optics parallel spectral domain optical coherence tomography for imaging the living retina,” Opt Express 13, 4792–4811 (2005). [PubMed: 19495398]
9. Zawadzki R, Jones S, Olivier S, Zhao M, Bower B, Izatt J, Choi S, Laut S, and Werner J, “Adaptive-optics optical coherence tomography for high-resolution and high-speed 3d retinal in vivo imaging,” Opt Express 13, 8532–8546 (2005). [PubMed: 19096728]

10. Leitgeb R, Schmetterer L, Drexler W, Fercher A, Zawadzki R, and Bajraszewski T, "Real-time assessment of retinal blood flow with ultrafast acquisition by color doppler fourier domain optical coherence tomography," Opt Express 11, 3116–3121 (2003). [PubMed: 19471434]
11. Makita S, Hong Y, Yamanari M, Yatagai T, and Yasuno Y, "Optical coherence angiography," Opt Express 14, 7821–7840 (2006). [PubMed: 19529151]
12. Jonnal RS, Kocaoglu OP, Wang Q, Lee S, and Miller DT, "Phase-sensitive imaging of the outer retina using optical coherence tomography and adaptive optics," Biomed Opt Express 3, 104–124 (2012). [PubMed: 22254172]
13. Merino D, Dainty C, Bradu A, and Podoleanu AG, "Adaptive optics enhanced simultaneous en-face optical coherence tomography and scanning laser ophthalmoscopy," Opt Express 14, 3345–3353 (2006). [PubMed: 19516479]
14. Pircher M, Zawadzki R, Evans J, Werner J, and Hitzenberger C, "Simultaneous imaging of human cone mosaic with adaptive optics enhanced scanning laser ophthalmoscopy and high-speed transversal scanning optical coherence tomography," Opt Lett 33, 22–24 (2008). [PubMed: 18157245]
15. Zawadzki RJ, Jones SM, Pilli S, Balderas-Mata S, Y Kim D, and Olivier SS, "Integrated adaptive optics optical coherence tomography and adaptive optics scanning laser ophthalmoscope system for simultaneous cellular resolution in vivo retinal imaging," Biomed. Opt. Express 2, 1674–1686 (2011). [PubMed: 21698028]
16. Hammer DX, Ferguson RD, Mujat M, Patel A, Plumb E, Iftimia N, Chui TYP, Akula JD, and Fulton AB, "Multimodal adaptive optics retinal imager: design and performance," JOSA A 29, 2598–2607 (2012). [PubMed: 23455909]
17. Meadway A, Girkin CA, and Zhang Y, "A dual-modal retinal imaging system with adaptive optics," Opt. Express 21, 29792–29807 (2013). [PubMed: 24514529]
18. Felberer F, Kroisamer J-S, Baumann B, Zotter S, Schmidt-Erfurth U, Hitzenberger CK, and Pircher M, "Adaptive optics SLO/OCT for 3d imaging of human photoreceptors in vivo," Biomed. Opt. Express 5, 439–456 (2014). [PubMed: 24575339]
19. Wells-Gray EM, Choi SS, Zawadzki RJ, Finn SC, Greiner C, Werner JS, and Doble N, "Volumetric imaging of rod and cone photoreceptor structure with a combined adaptive optics-optical coherence tomography-scanning laser ophthalmoscope," J. Biomed. Opt. 23, 1–15 (2018).
20. Liu Z, Tam J, Saeedi O, and Hammer DX, "Trans-retinal cellular imaging with multimodal adaptive optics," Biomed. Opt. Express 9, 4246–4262 (2018). [PubMed: 30615699]
21. Huber R, Wojtkowski M, , and Fujimoto JG, "Fourier domain mode locking (fdml): A new laser operating regime and applications for optical coherence tomography," Opt. Express 14, 3225–3237 (2006). [PubMed: 19516464]
22. Klein T, Wieser W, Eigenwillig CM, Biedermann BR, and Huber R, "Megahertz oct for ultrawide-field retinal imaging with a 1050 nm fourier domain mode-locked laser," Opt. Express 9, 3044–3062 (2011).
23. Azimipour M, Migacz JV, Zawadzki RJ, , Werner JS, and Jonnal R, "Functional retinal imaging using adaptive optics swept-source oct at 1.6mhz," Optica 6, 300–303 (2019).
24. Delori FC, Webb RH, and Sliney DH, "Maximum permissible exposures for ocular safety (ANSI 2000), with emphasis on ophthalmic devices," JOSA A 24, 1250–1265 (2007). [PubMed: 17429471]
25. Jonnal RS, Kocaoglu OP, Zawadzki RJ, Lee S-H, Werner JS, and Miller DT, "The cellular origins of the outer retinal bands in optical coherence tomography images," Invest Ophth Vis Sci 55, 7904–7918 (2014).
26. Migacz JV, Gorczynska I, Azimipour M, Jonnal R, Zawadzki RJ, and Werner JS, "Megahertz-rate optical coherence tomography angiography improves the contrast of the choriocapillaris and choroid in human retinal imaging," Opt. Express 15, 50–65 (2019).
27. Stevenson S and Roorda A, "Correcting for miniature eye movements in high-resolution scanning laser ophthalmoscopy," Proc. SPIE 5688, 145–151 (2005).
28. Azimipour M, Zwadzki RJ, Gorczynska I, Migacz JV, Werner JS, and Jonnal RS, "Intraframe motion correction for raster-scanned adaptive optics images using strip-based cross-correlation lag biases," PlosOne 113, 13138–13143 (2018).

29. Enoch JM, “Visualization of wave-guide modes in retinal receptors,” Am. J. Ophthalmol. 51, 1107–1118 (1961). [PubMed: 13696943]

30. Vohnsen B, Iglesias I, and Artal P, “Guided light and diffraction model of human-eye photoreceptors,” J. Opt. Soc. Am. A, Opt. Image Sci. Vis 22, 2318–2328 (2005). [PubMed: 16302385]

31. Putnam NM, Hammer DX, Zhang Y, Merino D, and Roorda A, “Modeling the foveal cone mosaic imaged with adaptive optics scanning laser ophthalmoscopy,” Opt. Express 18, 24902–24916 (2010). [PubMed: 21164835]

32. Miller DT, Cense B, Koperda E, Jonnal RS, and Gao W, “Does transverse chromatic aberration limit performance of AO-OCT retinal imaging?” in 1st Canterbury Workshop on Optical Coherence Tomography and Adaptive Optics, , vol. 7139 (International Society for Optics and Photonics, 2008), p. 71390Z.

33. Winter S, Sabesan R, Tiruveedhula P, Privitera C, Unsbo P, Lundstrom L, and Roorda A, “Transverse chromatic aberration across the visual field of the human eye,” J. Vis 16, 9–9 (2016).

34. Boehm AE, Privitera CM, Schmidt BP, and Roorda A, “Transverse chromatic offsets with pupil displacements in the human eye: sources of variability and methods for real-time correction,” Biomed. Opt. Express 10, 1691–1706 (2019). [PubMed: 31061763]

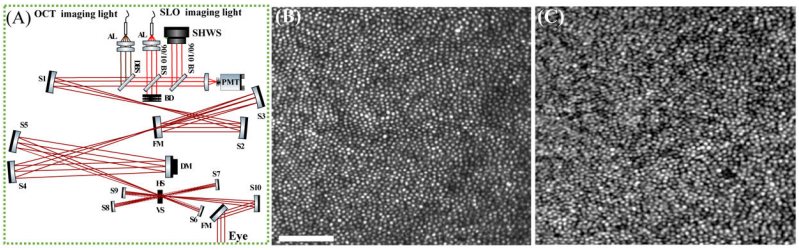

Fig. 1.

(A) Sample arm of the combined AO scanning system: DM, deformable mirror; SHWS, Shack-Hartmann wavefront sensor; AL, achromatic lens; S, spherical mirror; FM, flat mirror; BS, beam splitter; DBS, dichroic beam splitter; HS, horizontal scanner; VS, vertical scanner; BD, beam dump. Sub-pixel strip-based registration of the cone mosaics at 1.75°TR in a normal subject: panels **(B)** and **(C)** show an average of 50 motion-corrected cone mosaics acquired 1.75° temporal to the fovea simultaneously by SLO and OCT systems, respectively (Scale bar is 50μm across).

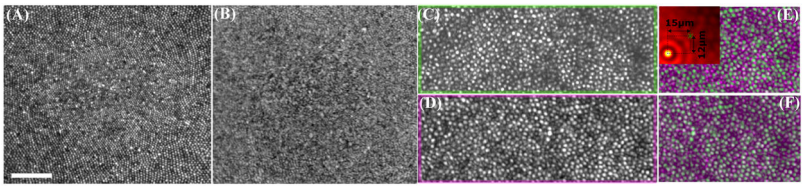

Fig. 2.

Panels **(A)** and **(B)** show an average of 50 motion-corrected cone mosaics at Fovea from the SLO and OCT channels, respectively (scale bar is 50μm across). Panel **(C)** and **(D)** show average of 50 motion-corrected cone mosaics at 3.5°TR from the SLO and OCT channels, respectively. Panel **(E)** and **(F)** a small field of view of SLO frame and OCT *en-face* image, color-coded and superimposed on top of each other before and after rigid-body registration, respectively. Panel **(E)** also shows the 2D crosscorrelation map of the SLO and OCT images. The offset could be the result of chromatic aberration, misalignment of the beams or perhaps offset of them respect to the center of pupil.

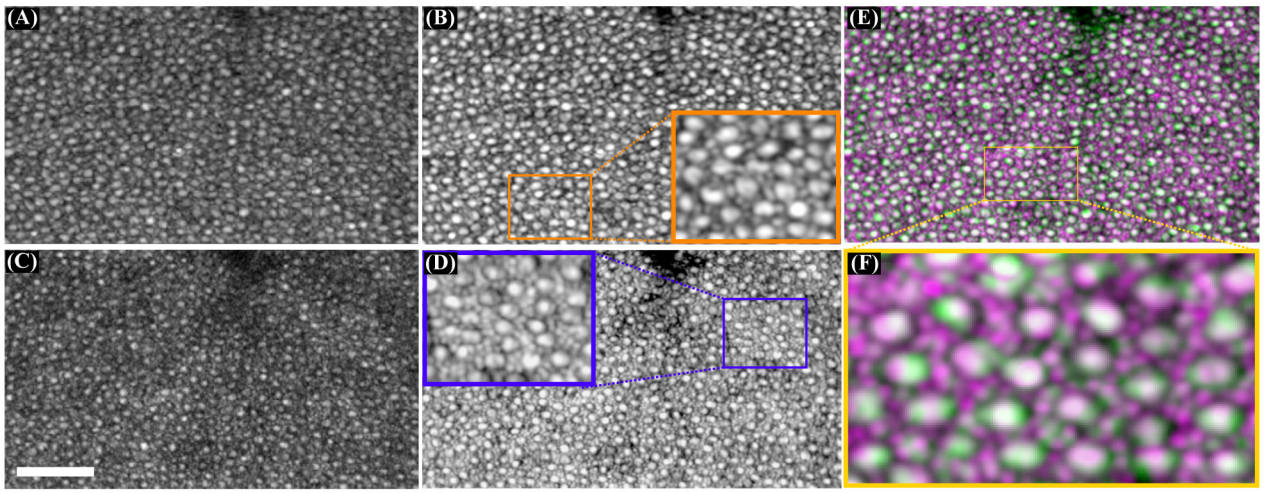

Fig. 3.

Volumes of a 1° × 1° patch acquired at 6°TR. **(A)** single and **(B)** motion-corrected average of 50 OCT en-face projections (logarithmic scale). Lower panel shows **(C)** single and **(D)** motion-corrected average of 50 SLO frames (logarithmic scale). **(E)** Superimposed color-coded OCT (green) and SLO (magenta) cone mosaics from panel **(B)** and **(D)**. **(F)** Magnified image of the marked area on panel **(E)** which shows the spatial correlation between rods and cones from the two imaging systems. Scale bar is 50μm across.

Table 1.

Specifications of the combined AO SLO/OCT system and scanning parameters during imaging.

FDML center wavelength	$1063 nm$
FDML spectral bandwidth (FWHM)	$78 nm$
FDML A-scan rate	$1.64 MHz$
OCT B-scan rate	$2 kHz$
Volume rate	$6 Hz$
Axial resolution in air	$10.8 \mu m$
FDML measured sensitivity	$-85.4 dB$
SLO light center wavelength	$840 nm$
SLO light spectral bandwidth (FWHM)	$50 nm$